Ann. Phys. (Leipzig) **15**, No. 7 – 8, 606 – 618 (2006) / **DOI** 10.1002/andp.200510205

Drude behavior in the far-infrared conductivity of cuprate superconductors

H.L. Liu[1,*], **M. Quijada**[1,**], **D.B. Romero**[1,***], **D.B. Tanner**[1,#], **A. Zibold**[1,°], **G.L. Carr**[2,§], **H. Berger**[3], **L. Forró**[3], **L. Mihaly**[4], **G. Cao**[5], **Beom-Hoan O**[6], **J.T. Markert**[6], **J.P. Rice**[7], **M.J. Burns**[8], and **K.A. Delin**[8]

[1] Department of Physics, University of Florida, Gainesville, FL 32611-8440, USA
[2] National Synchrotron Light Source, BNL, Upton, NY 11973, USA
[3] Ecole Polytechnique Fédérale, 1015 Lausanne, Switzerland
[4] Department of Physics, SUNY, Stony Brook, NY 11794, USA
[5] National High Magnetic Field Laboratory, Florida State University, Tallahassee, FL 32306, USA
[6] Department of Physics, University of Texas, Austin, TX 78712, USA
[7] Department of Physics and Materials Research Laboratory, University of Illinois at Urbana-Champaign, Urbana, IL 61801, USA
[8] Jet Propulsion Laboratory, California Institute of Technology, Pasadena, CA 91109, USA

Received 8 October 2005, accepted 17 January 2006
Published online 26 May 2006

Key words Infrared, Drude, cuprate.
PACS 74.72.-h, 74.25.-q, 71.27.+a

In commemoration of Paul Drude (1863–1906)

When viewed at frequencies below about 8 THz (250 cm^{-1}; 30 meV) the ab-plane optical conductivity of the cuprate superconductors (in their normal state) is well described by a Drude model. Examples include optimally-doped $YBa_2Cu_3O_{7-\delta}$ and $Bi_2Sr_2CaCu_2O_8$; even the underdoped phases have a Drude character to their optical conductivity. A residual Drude-like normal fluid is seen in the superconducting state in most cases; the scattering rate of this quasiparticle contribution collapses at T_c.

1 Introduction

The normal-state dc electrical resistivity in the ab plane of the cuprate materials is metallic, in the sense that it decreases with decreasing temperature [1]. Moreover, the magnitude of the dc resistivity, ∼200–300 $\mu\Omega$-cm at 300 K, is consistent with a picture of transport by a high density of mobile carriers. Consequently, it is natural to view the transport and optical properties in the context of a Drude model.

The Drude model is not adequate for the entire optical range, as there is known to be a strong absorption in the midinfrared spectral range; in addition, charge-transfer and interband transitions occur at higher

* Present address: Department of Physics, National Taiwan Normal University, 88, Sec. 4, Ting-Chou Road, Taipei 116, Taiwan E-mail: hliu@phy.ntnu.edu.tw
** Present address: NASA/GODDARD, MS 551 Greenbelt, MD 20771, USA E-mail: manuel.a.quijada@nasa.gov
*** Present address: NIST, 100 Bureau Drive, Stop 8441, Gaithersburg, MD 20899-8441, USA E-mail: dbromero@nist.gov
# Corresponding author E-mail: tanner@phys.ufl.edu
° Present address: Microelectronic Systems Division of Carl Zeiss, Carl Zeiss-Promenade 10, 07745 Jena, Germany E-mail: Axel.Zibold@t-online.de
§ E-mail: carr@bnl.gov

energies [2–4]. This midinfrared absorption [5] has been addressed either by including additional low-energy Lorentz oscillators in the conductivity model (a two-component picture) or by using a generalized Drude model with a frequency dependent scattering rate and effective mass (a one-component picture). The latter approach is the one more commonly used these days [4].

Despite this, if one restricts one's view to frequencies below about 8 THz (250 cm^{-1}; 30 meV) the ab-plane optical conductivity of the cuprate superconductors (in their normal state) is well described by a Drude model. Either of the above pictures predicts similar behavior in this case: the experiment is below the range of the Lorentz terms of the two-component picture and the frequency dependence of one-component models is eliminated when the frequency $\omega < k_B T/\hbar$ with T the temperature.

In this paper, we focus on the low-energy, ab-plane, normal-state optical conductivity of several cuprate superconductors. We discuss their behavior in terms of a Drude picture, and show that such a model gives a good description of the data in most cases.

2 The Drude conductivity

The Drude conductivity $\sigma(\omega)$ is

$$\sigma(\omega) = \frac{\omega_p^2 \tau}{4\pi(1 - i\omega\tau)} \tag{1}$$

where $\omega_p = \sqrt{4\pi n e^2/m}$ is the plasma frequency, with n the carrier density and m the effective mass, and τ the mean free time between collisions. In metals, where $T \ll T_F$, the mean free path ℓ is $\ell = v_F \tau$. (T_F is the Fermi temperature and v_F is the Fermi velocity.) This condition is met in the cuprates, though the Fermi velocity is about $10\times$ smaller than in simple free-electron metals. The dc conductivity is the $\omega \to 0$ limit of this equation, $\sigma_{dc} = \omega_p^2 \tau/4\pi = n e^2 \tau/m$. Good discussions of the optical properties of the Drude model are in Wooten [6] and in Dressel and Grüner [7].

The corresponding dielectric function is

$$\epsilon = \epsilon_\infty + \frac{4\pi i}{\omega}\sigma. \tag{2}$$

Here, ϵ_∞ contains the contributions of higher-lying interband and core-level transitions. From these equations, we can calculate the optical properties of a material once the parameters are known. From a different perspective, if the optical conductivity is measured, the data can be analyzed to obtain the scattering time τ (or scattering rate $1/\tau$) and the ratio of carrier density to effective mass, n/m. The latter quantity is usually called the oscillator strength or spectral weight, because the real part of the conductivity, $\sigma_1(\omega)$, satisfies the sum rule,

$$\int_0^\infty \sigma_1(\omega) = \frac{\pi}{2}\frac{n e^2}{m} \tag{3}$$

Figure 1 shows the real and imaginary parts of the optical conductivity, $\sigma_1(\omega)$ and $\sigma_2(\omega)$ respectively, calculated from the Drude model. The parameters are $\omega_p = 9800$ cm^{-1} and $1/\tau = 2.3T$, *i.e.,* linear in the temperature T. These parameters describe optimally doped $Bi_2Sr_2CaCu_2O_8$ and the a axis of $YBa_2Cu_3O_7$.

The real part of the conductivity, $\sigma_1(\omega)$, equals the dc conductivity at zero frequency, falls to half that value when $\omega = 1/\tau$, and follows a $1/\omega^2$ behavior at high frequencies. Note that as temperature is lowered, the curves become taller and narrower, and that the area under the curve is independent of τ, as shown by Eq. (3). $\sigma_2(\omega) = 0$ at zero frequency, rises linearly, is maximum when $\omega = 1/\tau$, and falls as $1/\omega$ at high frequencies. It is smaller than σ_1 at low frequencies and larger at high frequencies.

Two signatures of Drude-like metallic behavior are thus (1) a zero-frequency peak in σ_1 which narrows at low temperatures, and (2) a peak in σ_2 that moves to lower frequencies as temperature decreases.

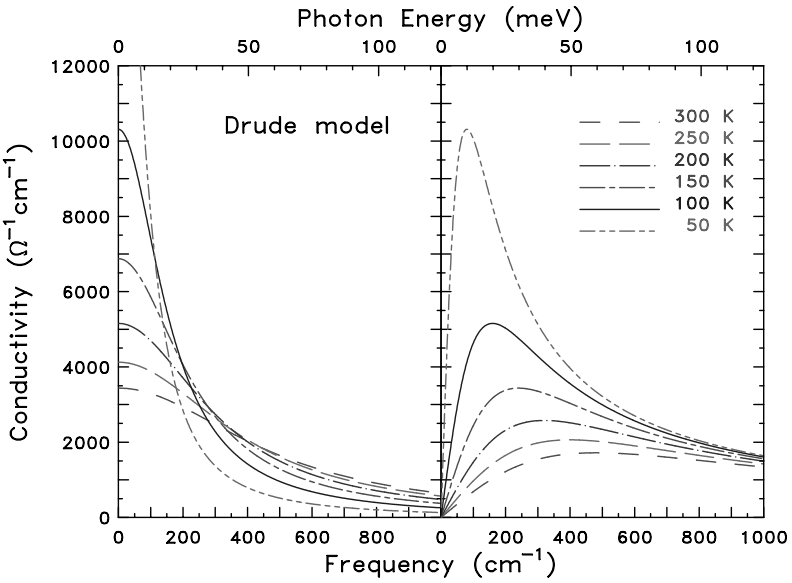

Fig. 1 (online colour at: www.ann-phys.org) Real (left panel) and imaginary (right panel) parts of the optical conductivity calculated from the Drude model.

3 Experiment

We studied single crystals of $YBa_2Cu_3O_{7-\delta}$ and $Bi_2Sr_2CaCu_2O_8$ and films of $YBa_2Cu_3O_{7-\delta}$. The preparation of the samples has been described elsewhere [8–15]. The samples have excellent quality surfaces, exhibit extremely low resistivity, and have sharp superconducting transitions. Crystal sizes ranged from 1×1 mm^2 to 6×4 mm^2; the $YBa_2Cu_3O_{7-\delta}$ films were 10×10 mm^2, quite thin (300–500 Å), and were deposited by pulsed-laser ablation on a $PrBa_2Cu_3O_{7-\delta}$ buffer layer on $YAlO_3$ substrates. The underdoped samples were $Bi_2Sr_2CaCu_2O_8$ or $YBa_2Cu_3O_{7-\delta}$ single crystals. The former had Y^{3+} substituted for Ca^{2+}, yielding [16] underdoped samples with $T_c = 35$ K (Pb 50%, Y 20%) and 40 K (Y 35%). In the $YBa_2Cu_3O_{7-\delta}$ system, we studied fully oxygenated $Y_{1-x}Pr_xBa_2Cu_3O_{7-\delta}$ single crystals in which substitution of Pr for the Y atom changes the hole content in the CuO_2 planes. The structure of the CuO chains remains unaffected [17]. The Pr-doped samples have a T_c of 92, 75, and 40 K, respectively, for $x = 0$, 0.15, and 0.35.

Normal-incidence reflectance or transmittance data were obtained using a modified Perkin-Elmer 16U grating spectrometer in the near-infrared through ultraviolet regions (2000–33,000 cm^{-1}). The far-infrared and midinfrared regions were covered using a Bruker IFS-113v Fourier transform spectrometer (80–4000 cm^{-1}). The transmittance of $Bi_2Sr_2CaCu_2O_8$ over 100–700 cm^{-1} was measured at beamline U4-IR of the National Synchrotron Light Source. For the single-domain samples, linear polarization of the light was achieved by placing a polarizer of the appropriate frequency range in the path of the beam using a gear mechanism that allowed in-situ rotation.

Low-temperature measurements (20–300 K) were done by attaching the sample holder assembly to the tip of a continuous-flow cryostat. A flexible transfer line delivered liquid helium from a storage tank to the cryostat. The temperature of the sample was stabilized by using a temperature controller connected to a previously-calibrated Si diode sensor and a heating element on the tip of the cryostat.

Reflectance spectra, $\mathcal{R}$ were measured at each temperature for both the sample and for a reference Al mirror. Division of the sample spectrum by the reference spectrum gave a preliminary reflectance of the sample. After measuring the temperature dependence of this preliminary reflectance for each polarization, the proper normalizing of the reflectance was obtained by taking a final room temperature spectrum, coating the sample with a 2000 Å thick film of Al, and remeasuring this coated surface. A properly normalized room-temperature reflectance was then obtained after the reflectance of the uncoated sample was divided by the reflectance of the coated surface and the ratio multiplied by the known reflectance of Al. This result was

then used to correct the reflectance data measured at other temperatures by comparing the individual room-temperature spectra taken in the two separate runs. This procedure attempts to correct for any misalignment between the sample and the mirror used as a temporary reference before the sample was coated and more importantly, it provides a reference surface of the same size and profile as the actual sample area. The uncertainties in the absolute value of the reflectance reported here are in the order of $\pm 1\%$. The error in the anisotropy is much smaller, $\pm 0.25\%$.

We measured the absolute transmittance $\mathcal{T}$ of free-standing single crystals at temperatures from 15 to 300 K. For metallic samples, the transmittance has the advantage of being less sensitive than the reflectance to systematic errors. Crudely speaking, this is because $\mathcal{T}$ is measured relative to 0% while $\mathcal{R}$ is relative to 100%, and it is hard to determine with great accuracy the 100% reference. The estimated error in our transmittance measurements is $\delta\mathcal{T} = \pm 0.0005$ below about 2000 cm^{-1}, increasing to ± 0.005 at higher frequencies. Since the signal transmitted by the sample is much weaker than the reference signal, we checked the linearity of the photodetector response with the intensity of the incident radiation. To minimize the effects of drifts in the spectrometer, sample and reference spectra were taken at each temperature.

4 Analysis of experimental data

We estimated the optical constants by Kramers-Kronig transformation of the reflectance data [6], the transmittance data [18], or from direct calculation when reflectance and transmittance are both measured [19].

The complex amplitude reflectivity coefficient $r(\omega)$ (the ratio of the reflected electric field to the incident electric field) is

$$r(\omega) = \rho(\omega)e^{i\theta(\omega)} = \frac{1-N}{1+N}, \tag{4}$$

where $\rho(\omega)$ is the amplitude and $\theta(\omega)$ the phase of the reflectivity coefficient. The complex refractive index $N(\omega)$, with real and imaginary parts $n(\omega)$, the refractive index, and $\kappa(\omega)$,the extinction coefficient, is the square root of the complex dielectric function $\epsilon(\omega)$,

$$N(\omega) = n(\omega) + i\kappa(\omega) = \sqrt{\epsilon(\omega)}. \tag{5}$$

A readily measured quantity is the reflectance, $\mathcal{R} = rr^* = \rho^2$. It is difficult to measure the phase $\theta(\omega)$ of the reflected wave, but the Kramers-Kronig procedure allows it to be calculated if the reflectance $\mathcal{R}(\omega)$ is known at all frequencies. Once we know both $\mathcal{R}(\omega)$ and $\theta(\omega)$, we use Eqs. (4) and 5 to obtain $N(\omega)$, $\epsilon(\omega)$, or $\sigma(\omega)$.

The Kramers-Kronig relations enable us to find the real part of the response of a linear passive system if we know the imaginary part of a response at all frequencies, and vice versa. We can apply the Kramers-Kronig relations to the amplitude reflectivity coefficient $r(\omega)$ viewed as a response function between the incident and reflected waves. An illuminating way to write the integral for the phase is

$$\theta(\omega) = -\frac{1}{2\pi}\int_0^\infty \ln\frac{|s+\omega|}{|s-\omega|}\frac{d\ln\mathcal{R}(s)}{ds}ds. \tag{6}$$

According to Eq. (6), spectral regions in which the reflectance is constant do not contribute to the integral. Further, spectral region $s \gg \omega$ and $s \ll \omega$ do not contribute much because the function $\ln|(s+\omega)/(s-\omega)|$ is small in these regions.

Formally, the phase-shift integral requires knowledge of the reflectance at all frequencies. In practice, one obtains the reflectance over as a wide frequency range as possible and then terminates the transform by extrapolating the reflectance to frequencies above and below the range of the available measurements. The conventional low-frequency extrapolation for metals is the so-called Hagen-Rubens relation, $\mathcal{R}(\omega) = 1 - A\sqrt{\omega}$, where A is a constant determined by the reflectance of the lowest frequency measured in the experiment.

For high-T_c samples, this procedure is inadequate; it can only be used as a first approximation. A better procedure extends the low-frequency data using fits of the data to a Drude-Lorentz model. The reflectance from this fit is then used as an extension below the lowest measured frequency. In the superconducting state, the reflectance is expected to be unity for frequencies close to zero. An empirical formula that represents the way $\mathcal{R}$ approaches unity is $\mathcal{R} = 1 - B\omega^4$, where B is a constant determined from the lowest frequency measured. However, it is better to use the same Drude-Lorentz model, but with the Drude scattering rate set to zero. The high frequency extrapolation has significant influence on the results, primarily on the sum rule derived from the optical conductivity. We reduced this effect by merging our data to vacuum ultraviolet spectra. At still higher frequencies, we terminated the transform using $\mathcal{R} \sim 1/\omega^4$, the free electron asymptotic limit.

Kramers-Kronig analysis is not as commonly applied to transmittance as it is to reflectance. Nevertheless, the transmittance of a film is subject to the same causality restrictions as the reflectance; consequently, one may estimate the phase shift on transmittance from a Kramers-Kronig integral, much as one does for reflectance. The requirements for utilizing this procedure are threefold. First, one needs a free-standing, uniform-thickness film with surfaces parallel to a fraction of the wavelength. In principal one could work with a thin film on a thick substrate, but the requirement on parallelism would become extreme, subsequent analysis would need to sort out the coherent multiple internal reflections in the substrate, and the spectral resolution would need to be good enough to measure these interference fringes. Second, wide spectral coverage is required. Third, reasonable photometric accuracy, $\mathcal{O}(1\%)$, is needed. Transmittance is easier than reflectance in this regard, because the results are far less sensitive to alignment and to inaccuracies in placement of reference.

After computing the phase, one may extract the complex refractive index (and all other optical constants) by numerical solution of

$$\sqrt{\mathcal{T}}e^{i\theta} = \frac{4N}{(N+1)^2e^{-i\delta} - (N-1)^2e^{i\delta}}, \tag{7}$$

where $\delta = \omega N d/c$, N is the complex refractive index, and is d the thickness of the film. An important detail is that the phase gained by the radiation in passing through a thickness d of vacuum must be added to δ before calculating N.

A third method of obtaining σ is to measure *both* transmittance and reflectance; from these two measurements one may calculate directly the real and imaginary parts of the conductivity. For a film which has thickness $d \ll \lambda$, the wavelength of the far-infrared radiation, and $d \ll \{\delta, \lambda_L\}$, the skin depth (normal state) or penetration depth (superconducting state), the transmittance across the film into the substrate and the single-bounce reflectance from the film are both determined by the film's dimensionless complex admittance y according to

$$\mathcal{T}_f = \frac{4n}{(y_1+n+1)^2 + y_2^2}, \tag{8}$$

and

$$\mathcal{R}_f = \frac{(y_1+n-1)^2 + y_2^2}{(y_1+n+1)^2 + y_2^2}, \tag{9}$$

where n is the refractive index of the substrate and y_1 and y_2 are respectively the real and imaginary parts of the admittance, which is related to the complex conductivity $\sigma = \sigma_1 + i\sigma_2$ of the film by $y = Z_0\sigma d$ where Z_0 is the impedance of free space ($4\pi/c$ in cgs; 377 Ω in mks). Although Eqs. (8) and 9 describe the physics of the thin film on a thick substrate, the external measured transmittance and reflectance are influenced by multiple internal reflections within the substrate (thickness x, refractive index n, and absorption coefficient α) and are equal to

$$\mathcal{T} = \mathcal{T}_f \frac{(1-\mathcal{R}_u)e^{-\alpha x}}{1 - \mathcal{R}_u\mathcal{R}_f' e^{-2\alpha x}}, \tag{10}$$

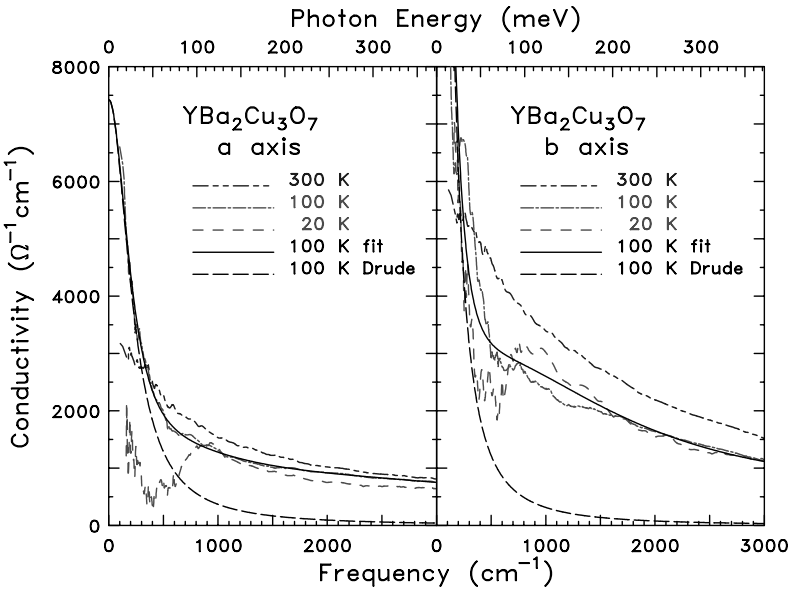

Fig. 2 (online colour at: www.ann-phys.org) Optical conductivity of $YBa_2Cu_3O_7$ at three temperatures for fields polarized along the a (left panel) and b (right panel) axes.

and

$$\mathcal{R} \approx \mathcal{R}_f + \frac{\mathcal{T}_f^2 \mathcal{R}_u e^{-2\alpha x}}{1 - \mathcal{R}_u \mathcal{R}_f^{'} e^{-2\alpha x}}, \tag{11}$$

where $\mathcal{R}_f^{'} = [(y_1 - n + 1)^2 + y_2^2]/[(y_1 + n + 1)^2 + y_2^2]$ is the substrate-incident reflection of the film, and $\mathcal{R}_u = [(1-n)^2 + \kappa^2]/[(1+n)^2 + \kappa^2] \approx [(1-n)/(1+n)]^2$ is the single-bounce reflectance of the substrate. The approximation holds when $\kappa = c\alpha/2\omega \ll n$ as is the case for weakly absorbing media. Measurements of $\mathcal{T}$ and $\mathcal{R}$ at each frequency determine σ_1 and σ_2. Beginning with the pioneering work of Palmer and Tinkham [19] this approach has been used a number of times to obtain the optical properties of thin films.

5 Results for optimally-doped samples

We begin with the far-infrared–midinfrared optical conductivity along the a and b axes of a single-domain $YBa_2Cu_3O_7$ crystal. The data, in Fig. 2, are shown up to 3000 cm^{-1} in order to illustrate the non-Dude midinfrared band. Two curves are measured above T_c (300 and 100 K) and one below (20 K). Also shown are fits using a two-component model (full line) and the Drude portion of this model (dashed line). Similar data have been shown by a number of groups [20–23].

The non-Drude character is seen most clearly by the minimal temperature dependence above about 1000 cm^{-1}. The dc conductivity is changing by almost a factor of 3 from 300 to 100 K whereas $\sigma_1(\omega > 1000\ \text{cm}^{-1})$ varies by only about 10%. In contrast, as can be seen by comparing to the fit, the normal-state data below about 300 cm^{-1} are well described by the Drude model. The dc intercept is about 3200 Ω^{-1}cm^{-1} (or $\rho = 310$ $\mu\Omega$-cm) at 300 K and 7500 Ω^{-1}cm^{-1} ($\rho = 130$ $\mu\Omega$-cm) at 100 K for $E \parallel a$ and 6000 Ω^{-1}cm^{-1} ($\rho = 170$ $\mu\Omega$-cm) at 300 K and 27,000 Ω^{-1}cm^{-1} ($\rho = 37$ $\mu\Omega$-cm) at 100 K for $E \parallel b$.

The superconducting-state data have a Drude-like upturn at the lowest frequencies. This residual absorption is seen in many cuprates below their transition temperature [20, 22, 24–26]. It can be described by a Drude model, with a much smaller spectral weight than above T_c.

The low frequency behavior in a $YBa_2Cu_3O_{7-\delta}$ thin film is shown in Fig. 3. Here, the conductivities were extracted from combined transmittance and reflectance measurements. Substrate phonon absorption

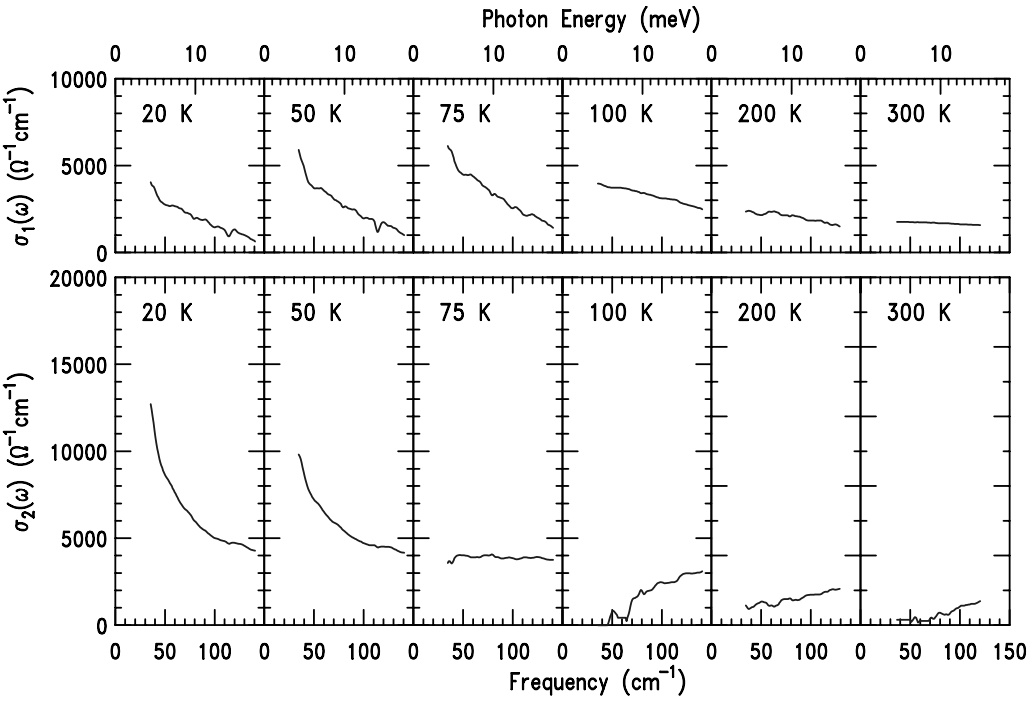

Fig. 3 (online colour at: www.ann-phys.org) The upper panels show the real part of the optical conductivity of a $YBa_2Cu_3O_{7-\delta}$ thin film at temperatures above and below T_c. The lower panels show the corresponding imaginary conductivity.

limits the data to frequencies below 120–150 cm^{-1}, depending on temperature. At 300 K, $\sigma_1(\omega)$ is very flat and is in accord with the dc resistivity, suggesting that the scattering rate is much larger than 120 cm^{-1}, as expected. $\sigma_2(\omega)$ increases more or less linearly with frequency, and is smaller than $\sigma_1(\omega)$. With decreasing $T > T_c$, $\sigma_1(\omega)$ grows and develops a negative slope, and $\sigma_2(\omega)$ also grows and the positive slope increases. At 100 K, $\sigma_1(150\ \text{cm}^{-1})$ is about half the dc intercept, suggesting that $1/\tau(100\ \text{K}) \approx 150\ \text{cm}^{-1}$.

Just below T_c (75 K), $\sigma_1(\omega)$ becomes obviously narrower, a behavior that we interpret as due to a collapse of the quasiparticle scattering rate in the superconducting state [18,27–30]. Finally at 50 K and 20 K, the Drude spectral weight decreases, as the condensate delta function at zero frequency [31] grows in strength. The delta function dominates $\sigma_2(\omega)$, giving it a $1/\omega$ behavior as expected from Kramers-Kronig. Still, a notable "normal-fluid" part remains below T_c [32].

$Bi_2Sr_2CaCu_2O_8$ also has a definite Drude-like character at low frequencies. Figure 4 shows the real and imaginary parts of the conductivity for a thin $Bi_2Sr_2CaCu_2O_8$ crystal, obtained from Kramers-Kronig analysis of transmittance. Only the normal-state data are shown. Temperature-dependent spectra of $Bi_2Sr_2CaCu_2O_8$ have been reported by a number of workers [18,33–35]. As temperature decreases, the Drude peak in $\sigma_1(\omega)$ grows higher and narrows. Note that with decreasing temperature, the low frequency conductivity increases and the high frequency conductivity decreases. The crossing of each curve with its neighbors occurs near or at the geometric mean of the relaxation rates, as expected for a Drude metal. The behavior of $\sigma_2(\omega)$ tells the same story, showing a peak that moves to lower frequencies as temperature decreases.

The data in Fig. 4 look a lot like the Drude curves in Fig. 1. This is no surprise, as the parameters were chosen from fits to these data. The 100 K fit and its Drude portion are also shown in Fig. 4. The fit to the data is good; the Drude curve separates from the data around 200 cm^{-1} and becomes a factor of two below it at 500 cm^{-1}.

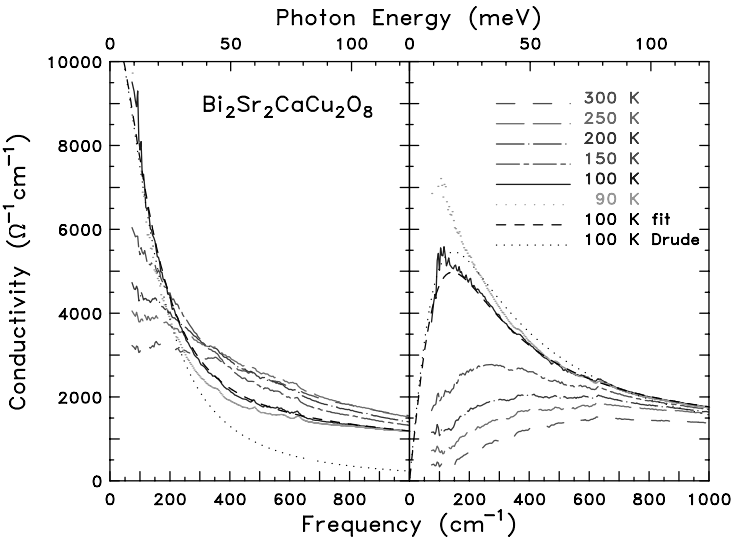

Fig. 4 (online colour at: www.ann-phys.org) Optical conductivity of $Bi_2Sr_2CaCu_2O_8$ at six temperatures above T_c. The left panel shows $\sigma_1(\omega)$ and the right panel shows $\sigma_2(\omega)$. Fits to the 100 K data are shown along with the Drude component of the conductivity.

6 Discussion for optimally-doped samples

One characteristic of the Drude picture of charge transport in metals is that the carrier density is temperature independent, so that the temperature dependence of the conductivity comes from the relaxation rate or mean free path's temperature dependence. The scattering of the charge carriers comes in part from their interaction with thermally-generated excitations in the metal, such as the phonons. The details of $1/\tau$ are governed by the details of the phonon density of states, the electronic band structure, and the electron-phonon coupling. At high temperatures, most of these details get washed out, and [36, 37]

$$\frac{\hbar}{\tau} = 2\pi\lambda k_B T + \frac{\hbar}{\tau_0}, \tag{12}$$

where λ is a dimensionless electron-phonon coupling parameter and $1/\tau_0$ the zero-temperature intercept, the residual scattering rate.

Fig. 5 shows the fitting parameters ω_{pD} and $1/\tau$ for the $Bi_2Sr_2CaCu_2O_8$ samples. The data come from a least-square minimization of fits to the measured transmittance. Error bars are shown, and are typically smaller than the plotted points. Very similar values have been found in single-domain $Bi_2Sr_2CaCu_2O_8$ crystals from transmittance [18] and reflectance studies [33]. Moreover, similar data for $YBa_2Cu_3O_{7-\delta}$ films has been shown by Gao *et al.* [27, 32] The plasma frequency is essentially constant until superconductivity sets in. The Drude plasma frequency falls once the superfluid density begins to build up; in these samples, it is immeasurably small below 50 K.

The normal-state scattering rate is linear and extrapolates to nearly zero at zero temperature, a remarkable behavior that is typically seen in the resistivity of optimally-doped crystals [1]. The slope (Eq. (12)) gives $\lambda = 0.37$. At the superconducting transition, the scattering rate, which represents the width of the low-energy Drude contribution below T_c, falls rapidly towards zero [18, 27–29].

7 Results for underdoped samples

The ab-plane far-infrared conductivity of optimally and underdoped $Bi_2Sr_2CaCu_2O_8$ is shown for several temperatures in Fig. 6. From left to right in the figure the data are for $T_c = 35$, 40, and 85 K respectively. The optical response of all samples is metallic, *i.e.,* when the temperature is lowered from 300 K, $\sigma_1(\omega)$ increases at the lowest frequencies, in accord with the dc resistivity. (Dc conductivity values, when known, are shown as squares at $\omega = 0$.) For $T > T_c$, $\sigma_1(\omega)$ is strongly suppressed in underdoped samples over the

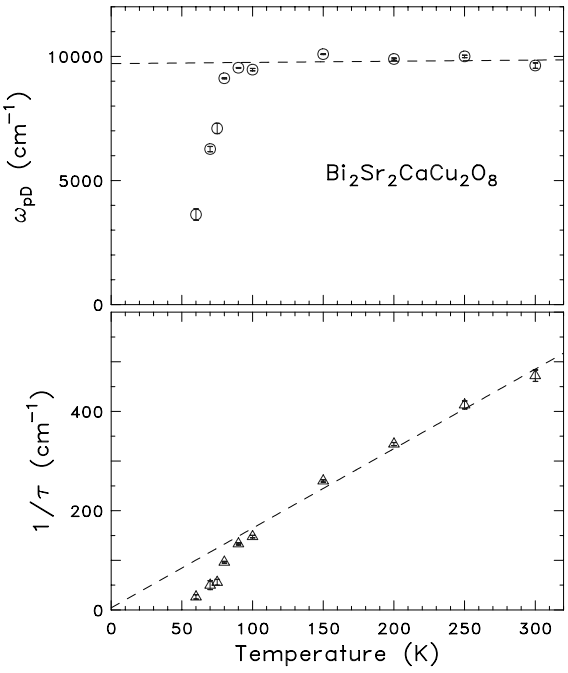

Fig. 5 (online colour at: www.ann-phys.org) The upper panel shows the Drude plasma frequency ω_p and the lower panel the Drude relaxation rate, $1/\tau$ as a function of temperature.

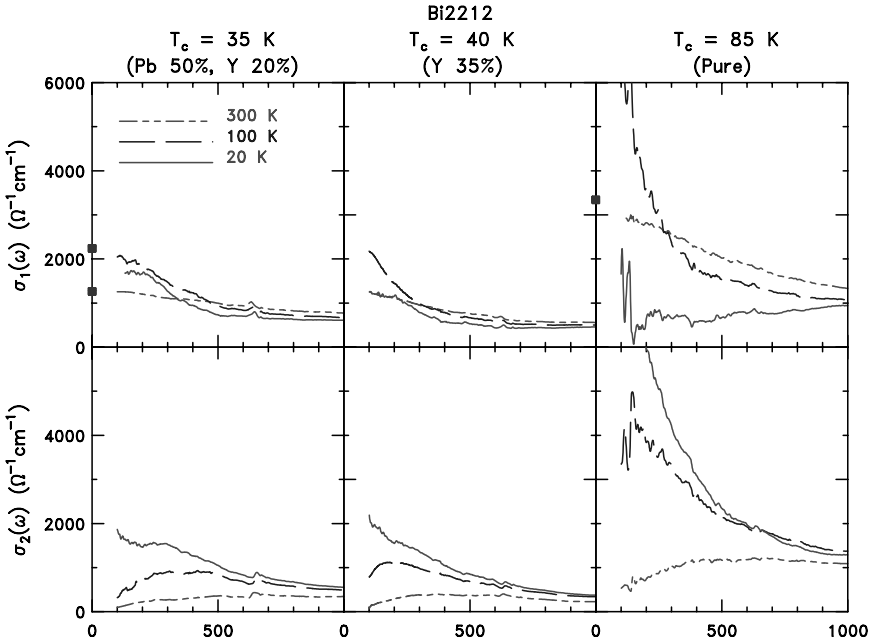

Fig. 6 (online colour at: www.ann-phys.org) Optical conductivity of optimally-doped (right panels) and underdoped (center and left panels) $Bi_2Sr_2CaCu_2O_8$. The upper row shows $\sigma_1(\omega)$ and the bottom row $\sigma_2(\omega)$.

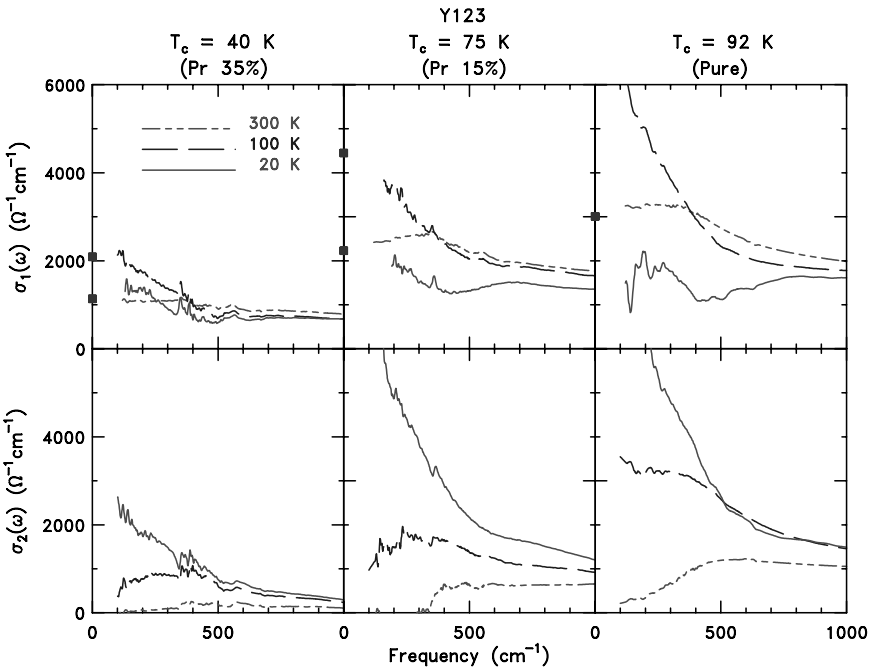

Fig. 7 (online colour at: www.ann-phys.org) Optical conductivity of optimally-doped (right panels) and underdoped (center and left panels) $YBa_2Cu_3O_{7-\delta}$. The upper row shows $\sigma_1(\omega)$ and the bottom row $\sigma_2(\omega)$.

entire infrared frequency range. Nevertheless, the conductivity below 300–400 cm^{-1} remains approximately Drude-like: a zero-frequency peak, which grows and sharpens as temperature is reduced toward T_c. The temperature dependence at frequencies above about 500 cm^{-1} is relatively modest; it is in fact mostly due to a narrowing of the Drude-like peak at zero frequency. Below T_c, there is a transfer of oscillator strength from the far-infrared region to the zero frequency δ-function response of the superconducting condensate [31]. The spectral weight lost at low frequencies in the superconducting state is large in the nearly optimally doped samples while in the most underdoped samples it is very small and a substantial Drude-like peak remains.

The lower row in Fig. 6 shows $\sigma_2(\omega)$ at three temperatures. As in the case of optimally doped samples, the imaginary part of the conductivity shows a maximum in the far infrared that shifts to lower energies at lower temperatures. As the temperature is lowered below T_c, $\sigma_2(\omega)$ develops a $1/\omega$ trend, with $\sigma_2 > \sigma_1$. This behavior indicates that the inductive current dominates the conduction current in the superconducting state. Here, the conductivity looks like that of perfect free carriers: $\sigma_2(\omega) = n_s e^2/m\omega$ The reduction of n_s in the underdoped samples is quite evident.

The temperature dependence of the ab-plane far-infrared conductivity of optimally and underdoped $YBa_2Cu_3O_{7-\delta}$ is shown in Fig. 7. From left to right in the figure the data are for $T_c = 40$, 75, and 92 K respectively. The optical response of all samples is metallic, *i.e.,* when the temperature is lowered from 300 K, $\sigma_1(\omega)$ increases at the lowest frequencies, in accord with the dc resistivity. (Dc conductivity values, when known, are shown as squares at $\omega = 0$.) For $T > T_c$, $\sigma_1(\omega)$ is strongly suppressed in underdoped samples. Nevertheless, the conductivity below 300–400 cm^{-1} remains approximately Drude-like, at least for the lower temperatures. $\sigma_1(\omega)$ at 300 K has a shoulder that is probably related to the non-Drude midinfrared absorption. Below T_c, there is a transfer of oscillator strength into the δ-function response of the superconducting condensate. The spectral weight lost at low frequencies in the superconducting state

is large in the nearly optimally doped samples while in the most underdoped sample it is very small and a substantial Drude-like peak remains.

The bottom row in Fig. 7 shows $\sigma_2(\omega)$. The imaginary part of the conductivity shows a maximum in the far infrared that shifts to lower energies at lower temperatures. Below T_c, $\sigma_2(\omega)$ develops a $1/\omega$ trend, indicating that the inductive current dominates the conduction current in the superconducting state. The reduced superfluid density is quite evident in the underdoped samples of Fig. 7.

8 Discussion for underdoped samples

The underdoped samples have a lower conductivity than do the optimally-doped samples. Now, the conductivity $ne^2\tau/m$ is controlled both by the low-energy spectral weight (n/m or ω_p^2) and by the scattering time τ. It is a reduction of spectral weight that causes the lower conductivity. Fits to the reflectance find values for the plasma frequencies, ω_p, and other transport properties, shown in Table I. These were found by fitting the reflectance to a Drude-Lorentz model, and using Eq. (12) to extract λ, and $1/\tau_0$ from the temperature-dependent scattering rate. These scattering rates are shown in Fig. 8. All the samples show a normal-state $1/\tau$ linear in T, with about the same slope, giving $\lambda \sim 0.35$.

Table 1 Drude plasma frequency, ω_p, coupling constant, λ, and the zero-temperature intercept, $1/\tau_0$, for six materials.

Materials	T_c (K)	ω_p (cm^{-1})	λ	$1/\tau_0$ (cm^{-1})
$Bi_2Sr_2CaCu_2O_8$	85	9000	0.40	9
Y 35%	40	5600	0.29	85
Pb 50%, Y 20%	35	6100	0.29	185
$YBa_2Cu_3O_{7-\delta}$	92	9800	0.38	2
Pr 15%	75	8700	0.36	135
Pr 35%	40	6800	0.38	252

Despite the large difference in T_c, the coupling constant λ is about the same in these materials. The scattering rates vary mostly in their intercept. The intercept is usually considered to be a measure of disorder in the sample. However, it is in no way clear that Matthiessen's rule [36], is applicable in these materials. Note, moreover, that the linear extrapolation passes well above the values of $1/\tau$ found below T_c.

It is interesting to compare the scattering rate with the dc resistivity data. The dc resistivity [38–40] of underdoped crystals is linear function in T for $T > T^*$, but shows a crossover to a steeper slope at $T < T^*$. If the temperature dependence of the normal-state resistivity $\rho = (m/ne^2)(1/\tau)$ were attributed entirely to the scattering rate, then the change at T^* would be attributed to the low-frequency, low-temperature suppression of the scattering rate. Because our measurements remain linear within error bars, they do not show any effect of the pseudogap. The linear-T behavior in $1/\tau$ is found in all samples, as shown in Fig. 8. The limited number of points and overall uncertainties of 3–5% prevent us from determining whether the observed deviation from linearity below T^* in dc resistivity data is seen in the scattering rate. However, a strong suppression in scattering, as suggested by some $1/\tau(\omega, T)$ results [25,41], is not observed in the Drude-like component of the optical conductivity.

9 Conclusions

The Drude model gives a good description of the low-energy, normal-state properties of the cuprates. So long as one's view does not extend much above 200–300 cm^{-1} (25–40 meV), the optical properties are dominated by the response of free carriers. The Drude contribution has nearly constant spectral weight as

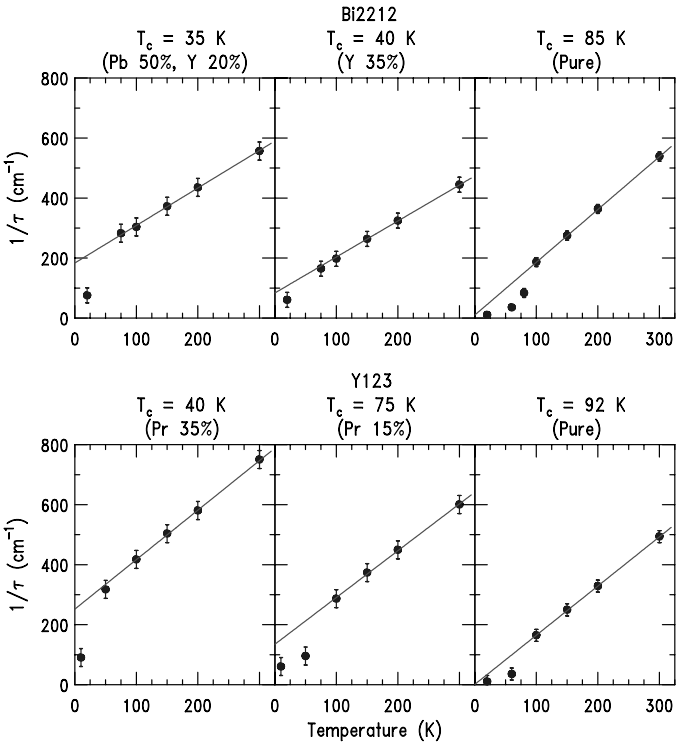

Fig. 8 (online colour at: www.ann-phys.org) Temperature-dependent Drude scattering rates for underdoped $YBi_2Sr_2CaCu_2O_8$ and optimally-doped $Bi_2Sr_2CaCu_2O_8$ (upper row) and underdoped $Y_{1-x}Pr_xBa_2Cu_3O_{7-\delta}$ and optimally-doped $YBa_2Cu_3O_{7-\delta}$ (lower row).

temperature is varied while the scattering rate is nearly linear in T. A residual Drude-like normal fluid is seen in the superconducting state; the scattering rate of this quasiparticle contribution collapses at T_c.

Acknowledgements This research was supported in part by the National Science Foundation through grant DMR-0305043 and by the Department of Energy through grant DE-AI02-03ER46070. Jack Crow kindly supplied the $Y_{1-x}Pr_xBa_2Cu_3O_{7-\delta}$ samples and Donald Ginsberg the single-domain $YBa_2Cu_3O_7$ crystals.

References

[1] M. Gurvitch and A.T. Fiory, Phys. Rev. Lett. **59**, 1337 (1987).
[2] T. Timusk and D.B. Tanner, in: Physical Properties of High Temperature Superconductors I, edited by D.M. Ginsberg (World Scientific, Singapore, 1989) p. 339.
[3] D.B. Tanner and T. Timusk, in: Physical Properties of High Temperature Superconductors III, edited by D.M. Ginsberg (World Scientific, Singapore, 1992) p. 363.
[4] D.N. Basov and T. Timusk, Rev. Mod. Phys. **77**, 721 (2005).
[5] K. Kamarás, C.D. Porter, M.G. Doss, S.L. Herr, D.B. Tanner, D.A. Bonn, J.E. Greedan, A.H. O'Reilly, C.V. Stager, and T. Timusk, Phys. Rev. Lett. **59**, 919 (1987); Phys. Rev. Lett. **60**, 969 (1988).
[6] F. Wooten, Optical Properties of Solids (Academic Press, New York, 1972).
[7] M. Dressel and G. Grüner, Electrodynamics of Solids (Optical Properties of Electrons in Matter) (Cambridge Press, Cambridge, 2002).
[8] J.P. Rice, D.M. Ginsberg, and M.W. Rabin, Phys. Rev. B **42**, 6217 (1990).
[9] P.D. Han and D.A. Payne, J. Cryst. Growth **104**, 201 (1990).
[10] D.B. Mitzi, L.W. Lombardo, A. Kapitulunik, S.S. Laderman, and R.D. Jacowitz, Phys. Rev. B **41**, 6564 (1990).
[11] L. Forro, D. Mandrus, R. Reeder, B. Keszei, and L. Mihaly, J. Appl. Phys. **68**, 4876 (1990).
[12] J.P. Rice and D.M. Ginsberg, J. Cryst. Growth **109**, 432 (1991).
[13] L.M. Paulius, B.W. Lee, M.B. Maple, and P.K. Tsai, Physica C **230**, 255 (1994).

[14] J. Ma, P. Alméras, R.J. Kelly, H. Berger, G. Margaritondo, X.Y. Cai, Y. Feng, and M. Onellion, Phys. Rev. B **51**, 9271 (1995).
[15] M.J. Burns, A.W. Kleinsasser, K.A. Delin, R.P. Vasquez, B.S. Karasik, W.R. McGrath, and M.C. Gaidis, IEEE Trans. Appl. Supercond. **7**, 3564–3567 (1997).
[16] T. Tamegai, K. Koga, K. Suzuki, M. Ichihara, F. Sakai, and Y. Iye, Jpn. J. Appl. Phys. **28**, L112 (1989).
[17] K. Takenaka, Y. Imanaka, K. Tamasaku, T. Ito, and S. Uchida, Phys. Rev. B **46**, 5833 (1992).
[18] D.B. Romero, C.D. Porter, D.B. Tanner, L. Forro, D. Mandrus, L. Mihaly, G.L. Carr, and G.P. Williams, Phys. Rev. Lett. **68**, 1590 (1992).
[19] L.H. Palmer and M. Tinkham, Phys. Rev **165**, 588 (1968).
[20] D.N. Basov, R. Liang, D.A. Bonn, W.N. Hardy, B. Dabrowski, M. Quijada, D.B. Tanner, J.P. Rice, D.M. Ginsberg, and T. Timusk, Phys. Rev. Lett. **74**, 598 (1995).
[21] N.L. Wang, S. Tajima, A.I. Rykov, and K. Tomimoto, Phys. Rev. B **57**, R11081 (1998).
[22] C.C. Homes, D.A. Bonn, R. Liang, W.N. Hardy, D.N. Basov, T. Timusk, and B.P. Clayman, 1999, Phys. Rev. B **60**, 9782 (1999).
[23] Y.S. Lee, K. Segawa, Y. Ando, and D.N. Basov, Phys. Rev. Lett. **94**, 137004 (2005).
[24] T. Pham, H.D. Drew, S.H. Moseley, and J.Z. Liu, Phys. Rev. B **41**, 11681 (1990).
[25] A.V. Puchkov, D.N. Basov, and T. Timusk, J. Phys.: Condens. Matter **8**, 10049 (1996).
[26] C. Bernhard, T. Holden, J. Humlícek, D. Munzar, A. Golnik, M. Kläser, Th. Wolf, L. Carr, C. Homes, B. Keimer, and M. Cardona, Solid State Commun. **121**, 93 (2001).
[27] F. Gao, G.L. Carr, C.D. Porter, D.B. Tanner, G.P. Williams, C.J. Hirschmugl, B. Dutta, X.D. Wu, and S. Etemad, Phys. Rev. B **54**, 700 (1996).
[28] I. Francois, C. Jaekel, G. Kyas, D. Dierickx, O. Van der Biest, R.M. Keeres, V.V. Moshchalkov, Y. Bruynseraede, H.G. Roskos, G. Borghs, and H. Kurz, Phys. Rev. B **53**, 12502 (1996).
[29] C. Ludwig, Q. Jiang, J. Kuhl, and J. Zegenhagen, Physica C **269**, 249 (1996).
[30] P.J. Turner, R. Harris, S. Kamal, M.E. Hayden, D.M. Broun, D.C. Morgan, A. Hosseini, P. Dosanjh, G.K. Mullins, J.S. Preston, R. Liang, D.A. Bonn, and W.N. Hardy, Phys. Rev. Lett. **90**, 237005 (2003).
[31] M. Tinkham and R.A. Ferrell, Phys. Rev. Lett. **2**, 331 (1959).
[32] F. Gao, G.L. Carr, C.D. Porter, D.B. Tanner, S. Etemad, T. Venkatesan, A. Inam, B. Dutta, X.D. Wu, G.P. Williams, and C.J. Hirschmugl Phys. Rev. B **43**, 10383 (1991).
[33] M.A. Quijada, D.B. Tanner, R.J. Kelley, M. Onellion, and H. Berger, Phys. Rev. B **60**, 14000 (1999).
[34] J.J. Tu, C.C. Homes, G.D. Gu, D.N. Basov, and M. Strongin, Phys. Rev. B **66**, 144514 (2002).
[35] J. Hwang, T. Timusk, and G.D. Gu, Nature **427**, 714 (2004).
[36] J.M. Ziman Principles of the Theory of Solids (Cambridge Press, Cambridge, 1964).
[37] P.B. Allen, T.P. Beaulac, F.S. Khan, W.H. Butler, F.J. Pinski, and J.C. Swihart, Phys. Rev. B **34**, 4331 (1986).
[38] B. Bucher, P. Steiner, J. Karpinski, E. Kaldis, and P. Wachter, Phys. Rev. Lett. **70**, 2012 (1993).
[39] B. Batlogg, H.Y. Hwang, H. Takagim, R.J. Cava, H.L. Kao, and J. Kwo, Physica C **130** 235–240 (1994).
[40] T. Ito, K. Takenaka, and S. Uchida, Phys. Rev. Lett. **70**, 3995 (1993).
[41] D.N. Basov, R. Liang, B. Dabrowski, D.A. Bonn, W.N. Hardy, and T. Timusk, Phys. Rev. Lett. **77**, 4090 (1996).

